Numerical study of wall effects on buoyant gas-bubble rise in a liquid-filled finite cylinder

Karthik Mukundakrishnan

Department of Anesthesiology and Critical Care, University of Pennsylvania, Philadelphia, Pennsylvania 19104, USA

Shaoping Quan

Department of Mechanical Engineering and Applied Mechanics, University of Pennsylvania, Philadelphia, Pennsylvania 19104, USA

David M. Eckmann

Department of Anesthesiology and Critical Care, University of Pennsylvania, Philadelphia, Pennsylvania 19104, USA

Portonovo S. Ayyaswamy*

Department of Mechanical Engineering and Applied Mechanics, University of Pennsylvania, Philadelphia, Pennsylvania 19104, USA

The wall effects on the axisymmetric rise and deformation of an initially spherical gas bubble released from rest in a liquid-filled, finite circular cylinder are numerically investigated. The bulk and gas phases are considered incompressible and immiscible. The bubble motion and deformation are characterized by the Morton number (Mo), Eötvös number (Eo), Reynolds number (Re), Weber number (We), density ratio, viscosity ratio, the ratios of the cylinder height and the cylinder radius to the diameter of the initially spherical bubble ($H^*=H/d_0$, $R^*=R/d_0$). Bubble rise in liquids described by Eo and Mo combinations ranging from (1,0.01) to (277.5,0.092), as appropriate to various terminal state Reynolds numbers (Re_T) and shapes have been studied. The range of terminal state Reynolds numbers includes $0.02 < Re_T < 70$. Bubble shapes at terminal states vary from spherical to intermediate spherical-cap–skirted. The numerical procedure employs a front tracking finite difference method coupled with a level contour reconstruction of the front. This procedure ensures a smooth distribution of the front points and conserves the bubble volume. For the wide range of Eo and Mo examined, bubble motion in cylinders of height $H^*=8$ and $R^* \geq 3$, is noted to correspond to the rise in an infinite medium, both in terms of Reynolds number and shape at terminal state. In a thin cylindrical vessel (small R^*), the motion of the bubble is retarded due to increased total drag and the bubble achieves terminal conditions within a short distance from release. The wake effects on bubble rise are reduced, and elongated bubbles may occur at appropriate conditions. For a fixed volume of the bubble, increasing the cylinder radius may result in the formation of well-defined rear recirculatory wakes that are associated with lateral bulging and skirt formation. The paper includes figures of bubble shape regimes for various values of R^*, Eo, Mo, and Re_T. Our predictions agree with existing results reported in the literature.

I. INTRODUCTION

The dynamics of gaseous-bubble motion in a viscous liquid medium has been studied over a number of years due to its importance in several areas of science, engineering, and technology. There is vast literature on the prediction of bubble terminal velocity, shape, and drag coefficient in such circumstances. A number of monographs and papers on this subject are available (see, for example, [1–10]). The study presented in this paper is motivated by applications in health sciences. In health sciences, gas-bubble motion in a viscous liquid is also of relevance in the study of gas embolism and decompression sickness. In this context, bubble motion in an arterial blood vessel has been experimentally and numerically investigated by a number of researchers [11–14]. However, the effects of buoyancy or the effects of high surface tension, high density, and high viscosity ratios that are more characteristic of gas-bubble motion in liquids have not been

fully explored. Furthermore, in gas embolism, the bubble sizes encountered are frequently of almost the same size as the vessel (occluding bubble). Analysis of bubble dynamics in such a situation would require the examination of wall effects in a significant way. In this paper, we focus on cylindrical wall effects on a buoyant bubble axisymmetrically rising in a fluid-filled finite cylinder. Nearly occluding bubbles are also studied.

The effect of radial wall location on the rate of rise of a single air bubble in four different quiescent liquids and different sized containers has been experimentally investigated in [15]. Low Mo fluids ranging from $O(10^{-5})$ to $O(10^{-11})$ are considered. Three different bubble regimes, namely, spherical, ellipsoidal (both stable and unstable), and spherical cap have been examined. The tube diameters and initial bubble radii are in the ranges 2.09–15 cm and 0.1–1.2 cm, respectively. A correlation has been proposed for the bubble terminal rise velocity as functions of the bubble to tube diameter ratio and an empirical constant. The constant is given graphically as a function of tube diameter and the surface tension of the liquid used. Very low Mo with small bubbles and very high Re preclude comparison of their results with those of the present study. Harmathy [16] has proposed correlations

*Author to whom correspondence should be addressed; ayya@seas.upenn.edu

for the wall effects on the terminal velocities of large bubbles and drops for Re=500. Coutanceau and Thizon [17] have investigated the wall effects in the creeping flow regime for bubble rise along the axis of a vertical circular tube filled with a highly viscous liquid using both theoretical and experimental procedures. They have concluded that the terminal speed of a spherical bubble is affected by the wall effect much sooner than its shape. Wall effects are shown to be profound under such circumstances. Our predictions are in accord with their reported results. Krishna *et al.* [18] have experimentally investigated the rise velocities of bubbles in the size range of 3–80 mm in cylindrical columns of varying diameters, and have observed increased drag and hence significant wall effects on bubbles moving in smaller diameter columns. We have favorably compared our predictions with their results.

In [19], the rise and deformation of a gas bubble in an otherwise stationary liquid contained in a closed, right vertical cylinder has been investigated using a modified volume-of-fluid (VOF) method. Bubble deformation, cusp formation, breakup and joining have been identified and discussed. Both two- and three-dimensional formulations have been examined. The various physical mechanisms associated with the computational results have been discussed. The results are shown to agree with experimental measurements, where available. One of the validations for the numerical method used in the present paper is based upon an excellent comparison between the result predicted here with that in [19] for identical conditions.

While it may be concluded that the cylindrical wall of a container tends to retard the motion, cause elongation of a fluid particle in the axial direction, and suppress secondary motion, there is insufficient experimental or numerical evidence detailing these aspects for the rise of gas bubbles in various liquids. In this numerical study, the effects of wall on the shape and the fluid field around a bubble rising in a liquid-filled finite cylinder are studied for various terminal shape regimes that a bubble would attain if it were rising in an infinite medium. Several numerical schemes for the study of free-surface flows are available. These include front-tracking or immersed-boundary [20–25], level set [26,27], phase-field [28], volume-of-fluid [29–31], coupled level-set and volume-of-fluid [32], immersed interface [33,34], ghost-fluid [35] methods, and moving mesh interface tracking [36]. In all methods except [36], flow discontinuities are smoothed and the surface tension force is distributed over a thin layer near the interface to become a volume force. The Navier-Stokes equation is then solved on a fixed Eulerian mesh. The present numerical study is based on a front-tracking method coupled with a level contour reconstruction procedure for periodic redistribution of the front points and reconstruction of a new front. In the front tracking method, an explicit background mesh of interconnected marker points is used to represent the interface. Such a Lagrangian representation of the interface allows an accurate calculation of the surface tension forces without the direct computation of the interface curvature.

Our numerical simulations have revealed that radial location of the cylindrical wall affects bubble rise velocities and shapes in a very significant manner.
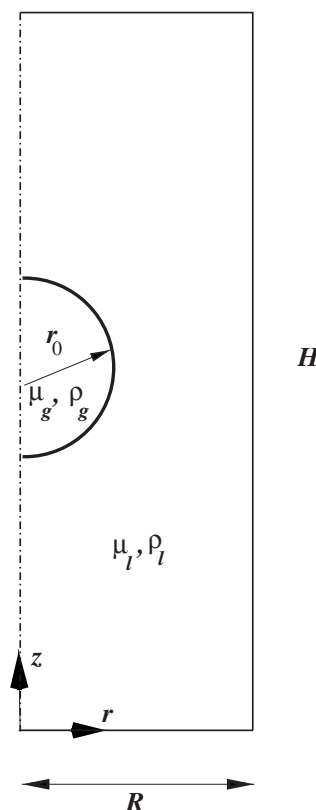

FIG. 1. Geometry of an axisymmetric bubble in a cylindrical tube.

II. MATHEMATICAL FORMULATION

The bubble motion is considered axisymmetric in (r,z) coordinates. The equations of motion for an isothermal, incompressible two-phase flow can be expressed by a single fluid continuum model as follows:

$$\boldsymbol{\nabla} \cdot \mathbf{u} = 0, \tag{1}$$

$$\rho\left(\frac{\partial \mathbf{u}}{\partial t} + \boldsymbol{\nabla}\mathbf{u} \cdot \mathbf{u}\right) = -\boldsymbol{\nabla} p + \boldsymbol{\nabla} \cdot \mu(\boldsymbol{\nabla}\mathbf{u} + \boldsymbol{\nabla}^T\mathbf{u})$$

$$+ \int_{S(t)} \sigma\kappa\mathbf{n}_f\delta(\mathbf{x} - \mathbf{x}_f)ds + \rho\mathbf{g}. \tag{2}$$

In the above, $\mathbf{u}$ is the fluid velocity, p is the dynamic pressure (total pressure minus the hydrostatic head), ρ and μ are the density and viscosity of the medium, $\mathbf{g}$ is gravitational acceleration, s is the arclength measure on the interface, κ is the curvature of the interface, σ is surface tension and is assumed to be a constant, $S(t)$ denotes the interface (time dependent), $\mathbf{n}_f$ denotes the unit normal vector on the interface (pointing into the bulk fluid), $\mathbf{x}_f$ denotes the position vector on the interface, and $\delta(\mathbf{x}-\mathbf{x}_f)$ stands for the δ function that is nonzero only when $\mathbf{x}=\mathbf{x}_f$. The gas-liquid system studied here is shown in Fig. 1. The cylinder is closed on all sides, and the top wall is sufficiently far away from the point of release of the bubble. In most of the computations, for a fixed height of the cylinder, the cylindrical wall is placed at varying radii in

order to study its effects on the motion and deformation of the gas bubble. The spherical bubble of diameter d_0 (radius r_0) is released from rest in a quiescent bulk fluid, and gravity is assumed to act in the negative z direction. The initial condition is

$$\mathbf{u}(r,z,t=0)=0. \tag{3}$$

The no-slip boundary conditions on the container walls are described by

$$\mathbf{u}(r,0,t)=\mathbf{0} \quad 0 \leq r \leq R, \tag{4}$$

$$\mathbf{u}(r,H,t)=\mathbf{0}, \quad 0 \leq r \leq R, \tag{5}$$

$$\mathbf{u}(R,z,t)=\mathbf{0}, \quad 0 \leq z \leq H, \tag{6}$$

where R is the radius, and H is the height of the cylindrical container. From the assumption of axial symmetry,

$$u(0,z,t)=0, \quad 0 \leq z \leq H,$$

$$\frac{\partial v}{\partial r}(0,z,t)=0, \quad 0 \leq z \leq H, \tag{7}$$

where u, v are the velocity components along the radial and axial directions, respectively.

The relevant nondimensional parameters employed in this study are, the Morton number (Mo), the Eötvös number (Eo), the Reynolds number (Re) based on the instantaneous velocity of the bubble centroid U_c, the density ratio of the bulk phase to the dispersed phase(ρ_l/ρ_g), and the viscosity ratio (μ_l/μ_g). The dimensionless numbers are defined by

$$\text{Re}=\frac{\rho_l U_c d_0}{\mu_l}, \quad \text{Eo}=\frac{(\rho_l-\rho_g)g d_0^2}{\sigma}, \quad \text{Mo}=\frac{g\mu_l^4(\rho_l-\rho_g)}{\rho_l^2\sigma^3}.$$

A terminal Reynolds number, $\text{Re}_T=\frac{\rho_l U_T d_0}{\mu_l}$, Bond number, $\text{Bo}=\frac{\rho_l g d_0^2}{4\sigma}$, and Weber number, $\text{We}=\frac{\rho_l U_T^2 d_0}{\sigma}$, are defined to compare our results with those in existing literature.

III. NUMERICAL METHODOLOGY

We now describe the numerical methodology employed for completeness.

In the bubble rise problem, the ratios of the properties of the two fluids across the interface (front) can be very large, for example, of the order of 1000 for density, and 100 for viscosity. Such sharp jumps in properties across the interface of ideally zero thickness complicate the numerical simulation due to instabilities. Also, the integration of the surface tension term in Eq. (2) introduces numerical difficulties if the sharp discontinuities are not resolved. To alleviate these problems, all the discontinuities in fluids' properties are first smoothed out across a finite thickness interface region, and the thickness of this region is proportional to the mesh size (diffused interface). Smoothing is achieved using a phase indicator function $I(r,z,t)$ (Heaviside function) whose value varies smoothly from 1 in the continuous (bulk) phase to 0 in the dispersed phase across the interface. The contour $I=0.5$

denotes the position of the interface. $I(r,z,t)$ is found by solving a Poisson equation given by (see [20,21,25] for more details)

$$\mathbf{\nabla} \cdot \mathbf{\nabla} I(r,z,t)=\mathbf{\nabla} \cdot \int_{S(t)} \mathbf{n}_f \delta(\mathbf{x}-\mathbf{x}_f)dS. \tag{8}$$

The sharp δ distribution in Eq. (8) is written as a product of two one-dimensional δ functions along the radial and axial directions. The one-dimensional δ function is numerically approximated as follows (see, [37]):

$$\delta(d)=\begin{cases} \delta_1(d), & |d| \leq 1, \\ 1/2-\delta_1(d), & 1<|d|<2, \\ 0, & |d| \geq 2. \end{cases} \tag{9}$$

and $\delta_1(d)=\frac{3-2|d|+\sqrt{1+4|d|-4d^2}}{8}$. Here, d denotes the distance from the origin of the source. Equation (8) is efficiently solved for the whole domain with appropriate boundary conditions using the HWSCRT code (cyclic reduction method) from FISH-PACK software library [38]. In our problem, a symmetry boundary condition $\frac{\partial I}{\partial r}=0$ is used at $r=0$ and a Dirichlet boundary condition with $I=1$ is used on all other boundaries. The material properties, namely, density and viscosity, of the single continuum fluid are then updated using the following equations (see, [39]):

$$\rho(r,z,t)=\rho_l I(r,z,t)+\rho_g[1-I(r,z,t)], \tag{10}$$

$$\frac{\rho}{\mu(r,z,t)}=\frac{\rho_l}{\mu_l}I(r,z,t)+\frac{\rho_g}{\mu_g}[1-I(r,z,t)]. \tag{11}$$

The surface tension force, $\mathbf{f}_{st}$, acting on a small segment of the interface surface is given as follows (see, [31]):

$$\mathbf{f}_{st}=\int_A^B \sigma\kappa\mathbf{n}_f ds=\sigma(\mathbf{t}_A-\mathbf{t}_B)-\mathbf{e}_r\sigma s_{AB}, \tag{12}$$

where $\mathbf{t}$ is the tangent vector on the interface, $\mathbf{e}_r$ is the unit radial vector, A, B are the end points of the interface segment, and s_{AB} is the length of the A-B segment. The calculated surface tension force on the marker points is then transferred to the fixed Eulerian cells [Eq. (2)] using a numerical approximation of the δ function. However, with such a distribution interfacial numerical instabilities arise for flows involving high surface tension forces coupled with large density and viscosity ratios. Such instabilities are a consequence of the distribution of large surface force to cells with very low liquid volume fractions. To avoid such instabilities, following [10], the surface tension force on each interfacial segment is distributed to the computational grid (i,j) in a "density-weighted" manner as follows:

$$\mathbf{F}_{st(i,j)}=\frac{\sum_e \rho_{i,j}\mathbf{f}_{ste}D_{i,j}(\mathbf{x}-\mathbf{x}_m)}{\sum_e \rho_{i,j}D_{i,j}(\mathbf{x}-\mathbf{x}_m)}, \tag{13}$$

where $\mathbf{x}=(i\Delta r,j\Delta z)$, $\mathbf{x}_m=(r_m,z_m)$ is the midpoint of the interfacial segment e, $\rho_{i,j}$ is the density at the given Eulerian grid point, and $D_{i,j}$ is

$$D_{i,j}(\mathbf{x} - \mathbf{x}_m) = \frac{\delta(r_m/\Delta r - i)\,\delta(z_m/\Delta z - j)}{2\pi r \Delta r \Delta z}. \tag{14}$$

The numerical approximation for each of the above one-dimensional δ function is given by Eq. (9).

The unsteady Navier-Stokes equations are discretized using a finite-difference-based variable density projection method described in [40–43]. The velocity, density, and viscosity are all located at cell centers. The lagged pressure $p^{n-1/2}$ is located at cell corners with the superscript n denoting the time level. The time stepping procedure is based on the Crank-Nicholson method.

Briefly, an intermediate velocity field is obtained using a semi-implicit viscous procedure: the equation for the intermediate velocity $\mathbf{u}^*$ is given as

$$\rho^{n+(1/2)}\left(\frac{\mathbf{u}^* - \mathbf{u}^n}{\Delta t}\right) = -\left[(\mathbf{u}\cdot\boldsymbol{\nabla})\mathbf{u}\right]^{n+(1/2)} - Gp^{n-(1/2)}$$
$$+ \left(\frac{D^* + D^n}{2}\right) + \mathbf{F}_{st}^{n+(1/2)} + \rho^{n+(1/2)}\mathbf{g}, \tag{15}$$

where Gp represents the pressure gradient operator, $D(\mathbf{u}) = \boldsymbol{\nabla}\cdot\mu(\boldsymbol{\nabla}\mathbf{u}+\boldsymbol{\nabla}^T\mathbf{u})$ represents the diffusion operator, and $\mathbf{F}_{st}$ represents the discretized surface tension forces. A second-order predictor-corrector method based on the unsplit Godunov method [44] is used to evaluate the advective terms $-[(\mathbf{u}\cdot\boldsymbol{\nabla})\mathbf{u}]^{n+(1/2)}$ and a standard second-order central finite difference is used to evaluate the diffusion terms $D(\mathbf{u})$. The resulting equations for the velocity components of $\mathbf{u}^*$ [Eq. (15)] are solved by a multigrid method based on red-black Gauss-Siedel (RBGS) iterations [45]. Note that $\mathbf{u}^*$ is not divergence free in general. Hence, a projection method is invoked on $\mathbf{u}^*$ to obtain the divergence-free velocity $\mathbf{u}^{n+1}$. The projection step is given by the following equations:

$$\frac{\mathbf{u}^{n+1} - \mathbf{u}^n}{\Delta t} = \mathcal{P}\left(\frac{\mathbf{u}^* - \mathbf{u}^n}{\Delta t}\right),$$

$$\frac{1}{\rho^{n+(1/2)}}Gp^{n+(1/2)} = \frac{1}{\rho^{n+(1/2)}}Gp^{n-(1/2)} + (I - \mathcal{P})\left(\frac{\mathbf{u}^* - \mathbf{u}^n}{\Delta t}\right), \tag{16}$$

where $\mathcal{P}$ represents the discretization of the projection operator. The details of the steps involved in discretization of individual terms in Eqs. (15) and (16) for an axisymmetric case and the corresponding time step restrictions for numerical stability are given in [32].

With the updated Eulerian velocity field, the front (marker) points are advected in a Lagrangian fashion as follows:

$$\mathbf{x}_f^{n+(1/2)} = \mathbf{x}_f^n + \mathbf{V}^n\frac{\Delta t}{2}. \tag{17}$$

$$\mathbf{x}_f^{n+1} = \mathbf{x}_f^{n+(1/2)} + \mathbf{V}^{n+1}\frac{\Delta t}{2}, \tag{18}$$

where $\mathbf{V}$ is bilinearly interpolated from the fluid velocities, and $\mathbf{x}_f$ denotes the position of the front point. Adding Eqs. (17) and (18), we get

$$\mathbf{x}_f^{n+1} = \mathbf{x}_f^n + \left(\frac{\mathbf{V}^{n+1} + \mathbf{V}^n}{2}\right)\Delta t. \tag{19}$$

Thus, Eq. (19) guarantees a second-order accurate scheme for the advection equation of marker points.

In this study, both redistribution of the front points and conservation of the bubble volume are simultaneously enforced using a level contour reconstruction procedure [20]. With a significantly deforming interface, a new distribution of front points is needed. The $I=0.5$ contour which also represents the interface, is first reconstructed in each cell using a simple linear interpolation of the contour value (a point-slope calculation). The intersection points of these linear contour segments with the background Eulerian cells now form the new representation of the front. Also, the volume fractions of the bubble and the bulk fluids in each of the cells intersected by the contour segments can be directly computed, and the total volume of the bubble estimated. However, in some simulations, $I=0.5$ contour may not always result in bubble volume conservation. For such cases, an optimum contour value, I_{opt}, different from 0.5 is found through iterations such that a desired level of accuracy for the total bubble volume conservation (typically within 0.5% of the initial volume of the bubble) is achieved. This is discussed in Sec. IV B. It is noted from our simulations that I_{opt} (where applicable) is only slightly different from 0.5. The interface reconstruction is done every few hundred time steps or more depending on the circumstance or when the volume loss of the bubble exceeds 0.5% of the original volume. This serves as the criterion for interface reconstruction.

For all the numerical simulations presented, a uniform nondimensional mesh size of 0.01 is employed in all simulations in both the radial and axial directions.

IV. RESULTS AND DISCUSSION

First, we validate the numerical procedure employed. Subsequently, we will investigate bubble rise in a range of parameter space, and compare our results with existing ones, where possible.

A. Validation of numerical predictions

In order to validate our numerical procedure, we first consider bubble rise in containers with two representative combinations of widely varying Eo and Mo fluids. We investigate conditions (cylinder sizes) where wall effects become negligible. For such circumstances, the numerical predictions are compared with experimental results obtained essentially for "infinite medium" conditions (negligible bounding wall effects) given in [1].

Bubble rise in cylinders of various heights $H^*=6$, 8, 10, 12, and for two different radii $R^*=3$, 4 are considered. The

TABLE I. Case (a) Eo=1.0, Mo=0.01. Here, $R^*=R_0/2r_0$, $H^*=H/2r_0$, $z_1^*=z_1/2r_0$, $z_2^*=z_2/2r_0$, and $U_T^*=U_T/(\frac{1}{3}\Delta\rho r_0^2 g/\mu_l)$. Also, $\mathrm{Re}_T=\frac{\rho_l U_T d_0}{\mu_l}$ and $\mathrm{Re}_{T\infty}$ is the experimental value.

R^*	H^*	z_1^*	z_2^*	U_T^*	Re_T	$\mathrm{Re}_{T\infty}$
4.0	12.0	4.0	10.0	0.64	0.52	0.54
4.0	10.0	3.75	8.5	0.64	0.52	0.54
4.0	8.0	3.2	6.1	0.64	0.52	0.54
4.0	6.0	1.55	3.84	0.64	0.52	0.54
3.0	12.0	4.2	10.0	0.62	0.51	0.54
3.0	10.0	3.75	7.8	0.62	0.51	0.54
3.0	8.0	3.2	6.1	0.62	0.51	0.54
3.0	6.0	1.55	3.84	0.62	0.51	0.54

fluid property values are such that Eo=1.0, Mo=0.01 and Eo=97.1, Mo=0.971, and $\rho_l/\rho_g=100$, $\mu_l/\mu_g=100$. Numerical computations for these parameters show that, for a given cylinder size, the bubble during its ascent, achieves a "terminal" velocity, $U_T^*=U_T/(\frac{1}{3}\Delta\rho r_0^2 g/\mu_l)$, a corresponding Reynolds number, Re_T, and a characteristic "terminal" shape. These are attained at a particular height, $z_1^*=z/d_0$, during its rise. The terminal velocity and the characteristic shape obtained at z_1^* are maintained up to a further height denoted by $z_2^*=z/d_0$, beyond which the effect of the top wall begins to influence the bubble motion and shape. We denote $z_2^*-z_1^*$ by Δz^*. Numerically computed values for z_1^* and z_2^* and terminal shapes are displayed in Tables I and II, and Figs. 2 and 3, respectively. We denote the terminal Reynolds number observed in experiments by $\mathrm{Re}_{T\infty}$. In Table I, the numerically predicted $\mathrm{Re}_T=0.51$ for $R^*=3$ and various H^* and $\mathrm{Re}_T=0.52$ for $R^*=4$ and various H^*, are in very good agreement with the experimental value of $\mathrm{Re}_{T\infty}=0.54$. In Table. II, predicted $\mathrm{Re}_T=18.0$ and this compares well with $\mathrm{Re}_{T\infty}=20$. In Figs. 2 and 3, the predicted spherical and the intermediate spherical-cap–skirted shapes are the same as those observed in experiments.

The distance over which the terminal velocities and shapes are maintained, Δz^*, are noted to increase with increasing values of H^* beyond 6. From Tables I and II, we note that for $H^*=6$ and $R^*\geq3$, and for the two combinations of Eo and Mo considered, the bubble motion results in the attainment of terminal velocity values and shapes corresponding to those in an infinite medium. However, in our

TABLE II. Case (b) Eo=97.1, Mo=0.971.

R^*	H^*	z_1^*	z_2^*	U_T^*	Re_T	$\mathrm{Re}_{T\infty}$
4.0	12.0	4.5	10.1	0.22	18.0	20
4.0	10.0	3.8	8.1	0.22	18.0	20
4.0	8.0	3.5	6.6	0.22	18.0	20
4.0	6.0	3.4	4.8	0.22	18.0	20
3.0	12.0	4.2	10.0	0.22	18.0	20
3.0	10.0	4.0	8.2	0.22	18.0	20
3.0	8.0	4.1	6.2	0.22	18.0	20
3.0	6.0	3.4	4.8	0.22	18.0	20

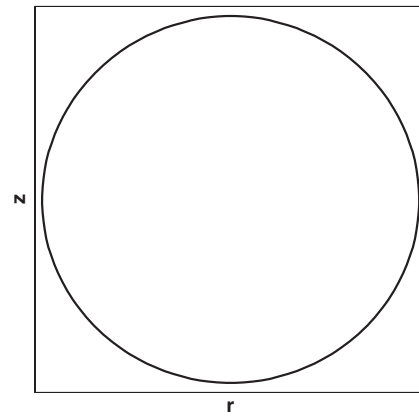

FIG. 2. Characteristic spherical shape of the bubble at the attainment of terminal velocity for Eo=1.0 and Mo=0.01. Here, $H^*=8$ and $R^*=3$.

subsequent computations, we will employ a fixed height of $H^*=8$ and vary R^* to evaluate cylindrical wall effects. This choice is based on our numerical experimentations from which we have concluded that for the large range of Reynolds numbers investigated ($0.03\leq\mathrm{Re}\leq70$), and for the wide range of Eo, Mo combinations studied [(1.0,0.01) to (277.5,0.092)], a value of $H^*=8$ is most appropriate. This H^* provides an adequate Δz^* enabling us to examine the roles of various forces at play in bubble ascension and deformation. Clearly, for $H^*=8$ and $R^*\geq3$ infinite medium conditions prevail within Δz^*.

In Fig. 4, the numerical results for bubble shapes and positions are shown at various nondimensional times, $\tau=t/\sqrt{r_0/g}$, for Eo=97.1, Mo=0.971, $H^*=8$ and for various radii $R^*=6$, 4, 3, 2, and 1. The experimentally observed terminal shape in an infinite medium for the Eo and the Mo values is a spherical-cap–skirted bubble [1]. For Figs. 4(a)–4(c) with $H^*=8$ and $R^*\geq3$, the bubble rise from z_1^* to z_2^*, essentially corresponds to that in an infinite medium. For example, in Fig. 4(b), $H^*=8$ and $R^*=4$, and from Table II, $z_1^*=3.5$ and $z_2^*=6.6$. The numerically predicted terminal shape in this range is noted to be a spherical-cap–skirted bubble, and this is in good agreement with experimental results for an infinite medium case. Beyond $z_2^*=6.6$, the bubble shape is noted to change as a consequence of the effects of the top containing boundary. In Fig. 4(c), $R^*=3$, the terminal state at $z_1^*=3.2$, is a spherical-cap–skirted bubble. In Figs.
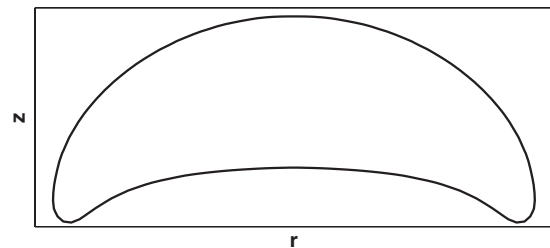

FIG. 3. Characteristic shape of an intermediate spherical-cap–skirted bubble at the attainment of terminal velocity for Eo=97.1 and Mo=0.971. Here, $H^*=8$ and $R^*=3$.
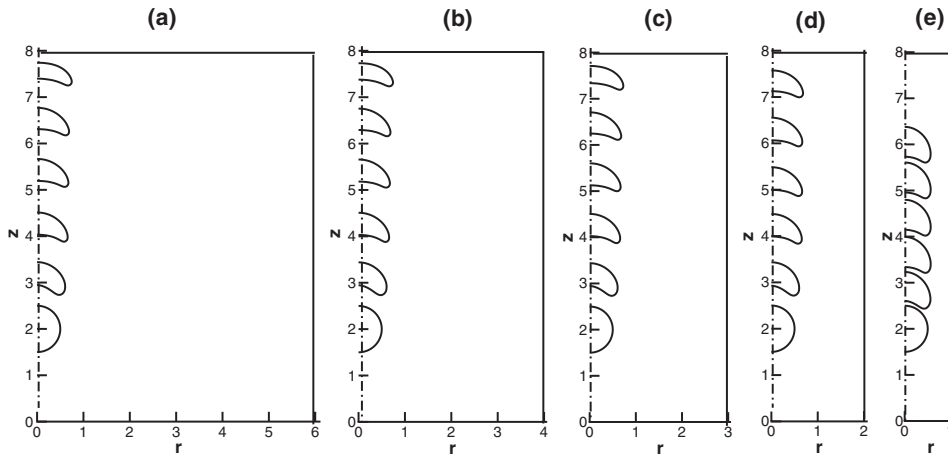
FIG. 4. Effects of changing R^* on the rising bubble shape: Mo =0.971, Eo=97.1. The aspect ratios H^*:R^* for (a), (b), (c), (d), and (e) are 8:6, 8:4, 8:3, 8:2, and 8:1, respectively. Figure drawn to scale and the right-hand boundaries represent cylinder walls in cases (a)–(e).

4(d) and 4(e), where $R^* < 3$, the cylindrical wall effects are noted to increasingly influence bubble motion and shape. Upon the attainment of terminal velocity, the shape of the bubble in Fig. 4(d), with $H^*=8$, $R^*=2$, is slightly different from those in Figs. 4(a)–4(c), but for the case of Fig. 4(e), with $H^*=8$, $R^*=1$, the wall effects are severe. The terminal dimpled ellipsoid shape at $R^*=1$ is distinctly different from the experimental results in an infinite medium. The instantaneous Reynolds numbers, for all the motions displayed in Figs. 4(a)–4(e), are shown in Fig. 5. Curves (a), (b), (c), (d), and (e) refer to the corresponding cases in Fig. 4. As would be expected, the terminal Reynolds numbers $Re_T \approx 18$ for cases (a), (b), and (c) are not different from each other because of negligible wall effect. But the terminal Re_T values for the cases (d) and (e) are lower [$Re_T=16.5$ for case (d), and $Re_T=12$ for case (e)]. The reduction in Re_T is directly attributable to increased total drag on the bubble due to the proximity of the cylindrical wall, and this feature will be explored in detail in a later section. We also note that bubbles achieve terminal state in shorter distances when R^* is reduced and the wall effects are pronounced. The terminal shapes are very different from those in an infinite medium.

As a second validation test, we evaluate terminal bubble shape at Eo=158.4 (Bo=39.6), Mo=0.065, $\mu_l/\mu_g=100$, and $\rho_l/\rho_g=1000$, with $H^*=8$ and $R^*=3$, and compare our predic-
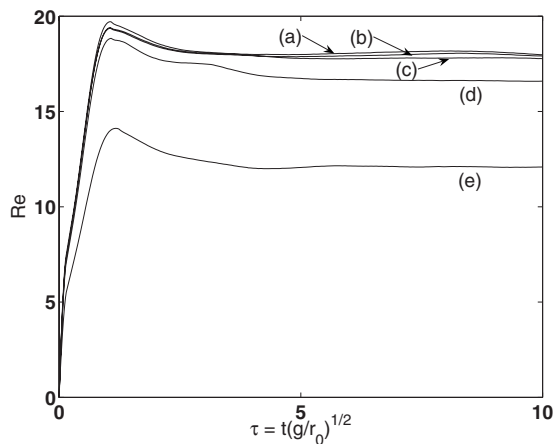
tions with the experimental results of Hnat and Buckmaster obtained using a cylindrical tank of 150 cm diameter and 150 cm height with a bubble volume of 0.94 ml for the same Eo and Mo [see, Fig. 1(a) in [46]]. The terminal bubble shape and the recirculatory wake structure obtained from numerical simulation are shown on the left-hand frame and compared with the experimental results shown on the right-hand frame in Fig. 6. Good agreement in the terminal shape and flow field are noted, although the value of $Re_{T\infty}$ as obtained in the experiment was 19.6 and that obtained numerically is 18.8. This is because of the fact that confinement effects due to the wall, however small, are still present. Complementary indications of this confinement effect with larger domains for the same physical problem were also noted in a recent study by Bonometti and Magnaudet [47].

We now consider a third validation test. The effects of the lateral walls on the rise velocities of a gas bubble in cylinders of various wall radii have been experimentally measured by Krishna *et al.* [18]. The experiments were carried out in seven cylindrical columns with different inside diameters varying from 0.01–0.63 m and heights varying from 1–6 m.

FIG. 5. Instantaneous Reynolds number corresponding to various cases given in Fig. 4.
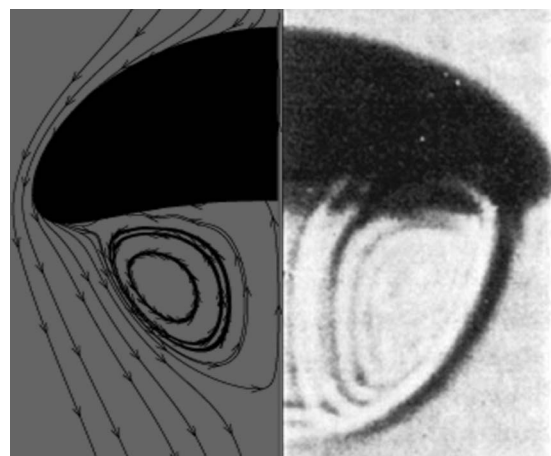

FIG. 6. Comparison of numerically predicted terminal bubble shape and wake structure with that of the experimental results given in [46][Fig. 1(a)]. Here, Eo=158.4 (Bo=39.6) and Mo=0.065. Left-hand frame, numerical prediction; right-hand frame, experimental results (Reprinted with permission from [46]. Copyright 1976, American Institute of Physics).
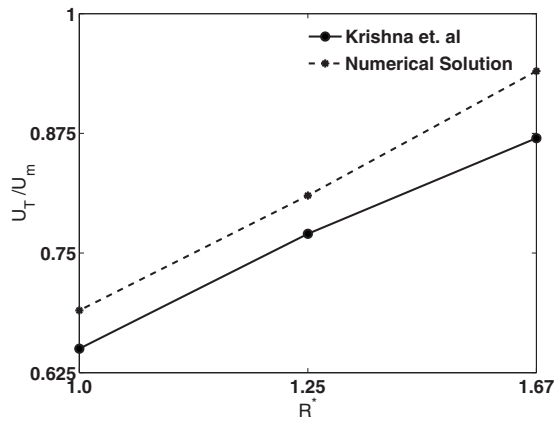
FIG. 7. Comparison of the numerical results of rise of air bubble in the presence of lateral walls with that of experimental results given in [18]. Here, $Mo=2.6\times10^{-11}$, $Eo=11$, and $1.0\leq R^*\leq1.67$.

The system studied was mostly air bubble in water and in one case, it is air bubble in Tellus oil. The bubble diameters were in the range of $3-79$ mm. For air-water system, the study corresponds to $Mo = 2.6\times10^{-11}$, and Eo in the range $1.2<Eo<850$. In Fig. 7, numerically predicted terminal velocities corresponding to $Eo = 11$ and $Mo = 2.6\times10^{-11}$ are compared with those observed in the experiments. We choose to display comparison in the range $1.0\leq R^*\leq1.67$, for illustration. In Fig. 7, the ordinate is a dimensionless velocity that is the ratio of bubble terminal velocity U_T to U_M. U_M is the velocity predicted by Mendelson equation [48] and is given by $U_M=\sqrt{\frac{2\sigma}{\rho_l d_0}+\frac{gd_0}{2}}$. The predicted results compare with experimental values to within 10% noting that the experiments reported in [18] are carried out in very long open cylinders.

These various comparisons serve to validate our numerical procedure.

B. Volume conservation of bubble phase

Volume conservation of bubble phase in numerical simulations of two-phase flow is a very important requirement. Volume gain or loss may affect the shape of the interface and also the dynamics of the problem. The details as to how we ensure bubble volume conservation in our numerical model has been described in Sec. III. Here, we demonstrate the satisfaction of this requirement by an illustrative simulation. Figure 8 shows a comparison between bubble shapes for identical release conditions and subsequent nondimensional times as computed without a bubble volume conservation scheme [Fig. 8(a)], and with the volume conservation scheme [Fig. 8(b)], incorporated into the numerical procedure. The nondimensional parameters for this simulation are $\mu_l/\mu_g=\rho_l/\rho_g=80$, $Mo=1.2\times10^{-3}$, and $Eo=200$. These parameters are the same as those used in Fig. 10 of Ref. [19] and case (b). Bubble shapes and positions are displayed for $\tau=0$, 1, 2, and 2.24. Predictions in Fig. 8(b) are in excellent agreement with the predictions in [19]. As time progresses, in Fig. 8(a), the lower surface of the bubble approaches the top surface at a faster rate than in the corresponding one
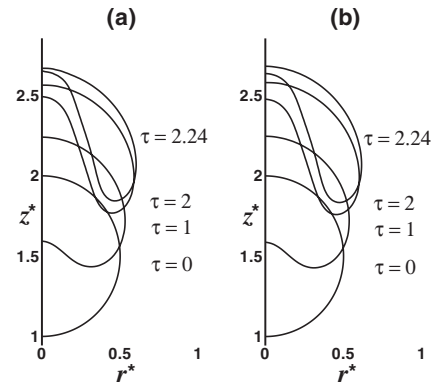

FIG. 8. Bubble positions for $\frac{\mu_l}{\mu_g}=\frac{\rho_l}{\rho_g}=80$, $Mo=1.2\times10^{-3}$, and $Eo=200$. (a) Without conservation scheme, (b) with conservation scheme. The nondimensional times of the bubble positions from the bottom are $\tau=0$, 1, 2, 2.24, respectively.

shown in Fig. 8(b). This is a consequence of an over prediction of the liquid jet strength by the scheme that does not conserve bubble volume. The toroidal vortex strength on the bottom surface of the bubble is over predicted. The scheme lacking accurate volume conservation will therefore incorrectly predict the penetration of the upper surface of the bubble by the lower surface leading to bubble breakup at an earlier time. Since bubble breakup introduces new dynamics, it is important to know its occurrence in precise terms. This emphasizes the need for an accurate volume conservation procedure in numerical schemes such as the one employed here.

In Fig. 9, as another test of accuracy of the bubble volume conservation scheme, we display the relative error in the bubble volume prediction for the case where $Eo=97.1$ and $Mo=0.971$, and $H^*=8$ and $R^*=3$. As the bubble ascends, the instantaneous bubble volumes at selected time intervals are calculated. This volume is compared with the initial bubble volume. The bubble volume loss is then calculated using the following formula: bubble volume error $=$ [(instantaneous volume-initial volume)/initial volume] $\times100$. In Fig. 9, we display the error as a function of time, τ, at eight different
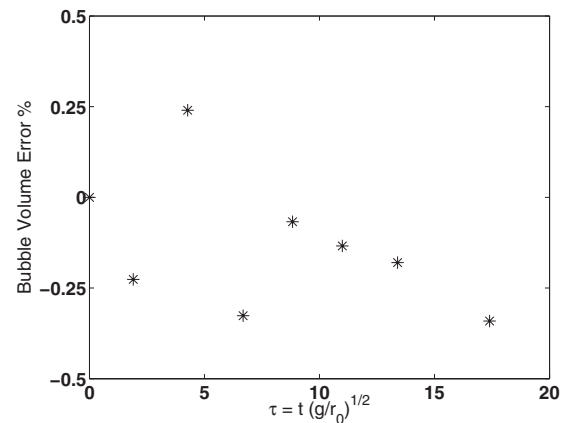

FIG. 9. Bubble volume conservation with the level-contour reconstruction procedure. $Eo=97.1$, $Mo=0.971$.

TABLE III. Various regimes chosen for numerical simulations. $\mathrm{Re}_{T\infty}$ and the terminal shape descriptions from [1] are displayed.

Regime	Terminal shape in infinite medium	Eo	Mo	$\log_{10} \mathrm{Mo}$	$\mathrm{Re}_{T\infty}$
(a)	Spherical	20	10	1.0	1.5
(b)	Ellipsoidal	10	0.01	−2.0	11.0
(c)	Dimple ellipsoidal cap	185.5	330	2.52	5.5
(d)	Spherical cap	54.4	0.0026	−2.58	60.0
(e)	Intermediate spherical-cap–skirted	277.5	0.092	−1.04	80.0

values, including at $\tau=0$. The instantaneous volume of the rising bubble is noted to be conserved very well within 0.5% of the original volume.

C. Detailed study of cylindrical wall effects

In this section, the effects of cylindrical wall of the finite cylinder on the terminal rise velocities and characteristic shapes of a gas bubble are evaluated for a fixed $H^*=8$, and for R^* values of 2, 1, 0.75, 0.6, and 0.55. The values of Eo-Mo combinations for these simulations are so chosen that they correspond to five different terminal shapes of a gas-bubble rising in an infinite medium [1]. The terminal shapes chosen are spherical, ellipsoidal, dimpled-ellipsoidal cap, spherical cap, and intermediate spherical-cap–skirted. The values of Eo-Mo combinations and the descriptions of corresponding terminal bubble shapes in infinite media are shown in Table III.

1. Terminal bubble shapes

A bubble, immediately after release, rises up rapidly due to buoyancy force, and a fluid jet forms at the bottom of the bubble. The jet tends to push the lower surface of the bubble up towards the top surface. The jet formation is a consequence of mass conservation in the liquid medium. The liquid jet initially accelerates accompanied by a curving of the lower surface of the bubble. There will be an increased surface tension force due to increased curvature, and an increased viscous drag, both opposing the effect of the jet. As a consequence, the bubble will start to decelerate until a force equilibrium between inertia, viscous, and surface ten-
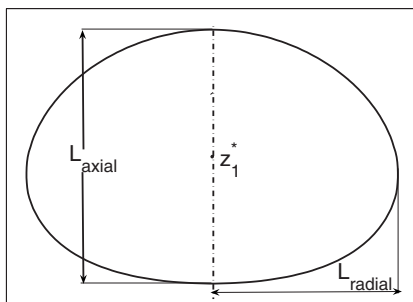
sion forces is attained where upon the bubble will attain a terminal shape and translate at a constant terminal velocity. For cases where viscous forces in the bulk fluid are dominant (for example, at low Reynolds number), a clean bubble in an infinite medium will remain spherical independent of the magnitude of the surface tension force. However, for bubble motion in a finite cylindrical vessel, slight deformation occurs even at low Reynolds number and this can be attributed to wall effects.

In order to quantitatively characterize deformation, a deformation parameter is defined here as the ratio of the maximum length of the bubble along the axial $(z-)$ direction, L_{axial}, to that of 2 times the maximum length along the radial direction, L_{radial}, when the bubble attains its terminal shape (at z_1^*) (see, Fig. 10). For purposes of comparison, a second deformation factor called the "geometric deformation factor" is also evaluated. This factor denotes the deformation of a spherical bubble that remains stagnant in a cylindrical tube of given radius, R. For $R^* \geq 0.5$, the geometric deformation factor of a sphere is equal to 1 (remains undeformed) and for $R^* < 0.5$, it attains the shape of a cylindrical bubble with hemispherical end caps of radii equal to cylinder radius in accord with its volume conservation.

The numerically evaluated bubble deformation factors, $L_{\mathrm{axial}}/(2L_{\mathrm{radial}})$, as functions of R^*, for various regimes (see Table III) are shown in Fig. 11 along with the deformation factor for a stagnant bubble (dashed-dotted line).

For case (a), Eo, Mo=20, 10, $\mathrm{Re}_{T\infty}=1.5$, and the terminal shape in an infinite medium is spherical. For $R^*=2$, the ter-

FIG. 10. Schematic of the lengths used in defining the deformation factor for the bubble. A representative terminal bubble shape is shown.
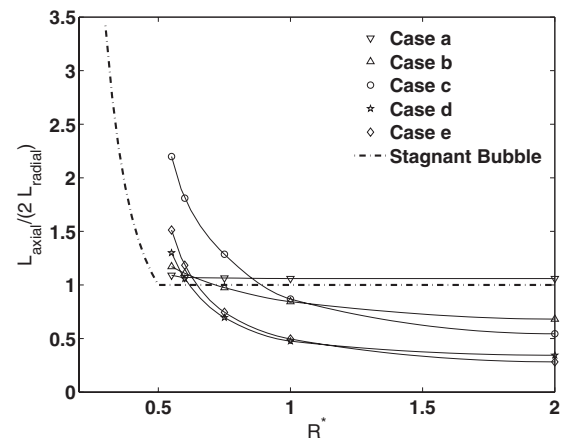

FIG. 11. Deformation factor for bubbles in different regimes. Legend details for cases (a)–(e) are given in Table III. $H^*=8$, for all cases.
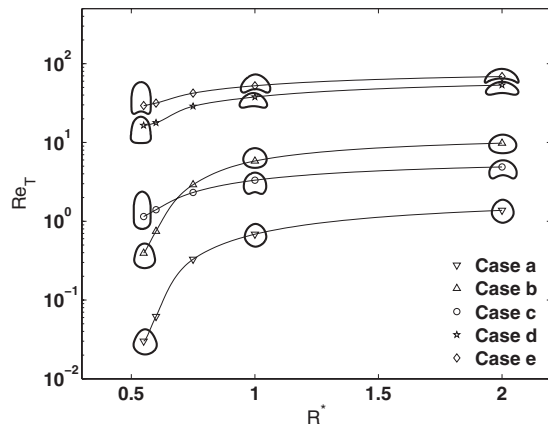
FIG. 12. Values of Re_T for various dimensionless wall distances. See Table III for legend details.

FIG. 13. Re_T–We space spanned by the bubbles in various regimes. The values of Re_T and We decrease as the wall proximity increases for each case. See Table III for legend details.

minal shape is nearly spherical, and Re_T is 1.4 and We $=1.3$ (see, Figs. 11–13). The viscous, inertial, and surface tension forces are of the same order $[\sim O(1)]$. Deformation by inertial forces is resisted both by viscous and surface tension forces. In the range, $R^*=2$ to $R^*=0.55$, the deformation continues to be small (Fig. 12) with a slight elongation occurring in the axial direction. The deformation factor is essentially constant (Fig. 11) and is slightly above one. The terminal Reynolds number decreases from 1.4 at $R^*=2$ to 0.68 at $R^*=1$ to 0.03 at $R^*=0.55$, the majority of decrease occurring for $R^*<1$. For $R^*<1$, the drag due to wall effects are severe. At low Reynolds number, spherical bubbles in closed cylindrical containers experience slight deformation as a result of wall effects. However, the deformation is only slight even with increased radial wall effects. These observations are in accord with the results reported in [17].

For case (b), Eo, Mo$=10$, 0.01, $\mathrm{Re}_{T\infty}=11.0$, and the terminal shape in an infinite medium is ellipsoidal. For $R^*=2$, the terminal shape continues to be ellipsoidal, and Re_T is 9.8 and We$=3.0$ (see, Figs. 11–13). Inertial forces and surface tension forces are of the same order and are higher than viscous forces. In the front, surface tension forces act to maintain a spherical shape, whereas inertial (dynamic) forces act to flatten, and hydrostatic forces act to elongate. The final ellipsoidal shape of the particle is determined by a balance of these three effects. For $R^*<2$, the bubble becomes nearly spherical with increasing radial wall proximity, and at $R^*=0.55$, assumes an elongated shape whose trailing end is flatter while the leading end is sharper (Fig. 12). The axial length of the bubble is increased. The deformation factor increases with decreasing R^* in a linear manner from $R^*=2$ to $R^*=1$. Subsequently, the increase in the deformation factor occurs with a higher slope (Fig. 11). The curvature of the leading end is higher compared to that at the rear. Re_T decreases from 9.8 at $R^*=2$ to 5.8 at $R^*=1$. For $R^*<1$, the Reynolds number drastically decreases from a value of 5.8 at $R^*=1$ to 0.39 at $R^*=0.55$ (Fig. 12). From Fig. 13, the We decreases from 3 to 0.005. This is because, for $R^*<1$, the wall effects increases the drag and significantly slows down the speed of the bubble.

For case (c), Eo, Mo$=185.5$, 330, $\mathrm{Re}_{T\infty}=5.5$, and the terminal shape in an infinite medium is a dimpled ellipsoidal
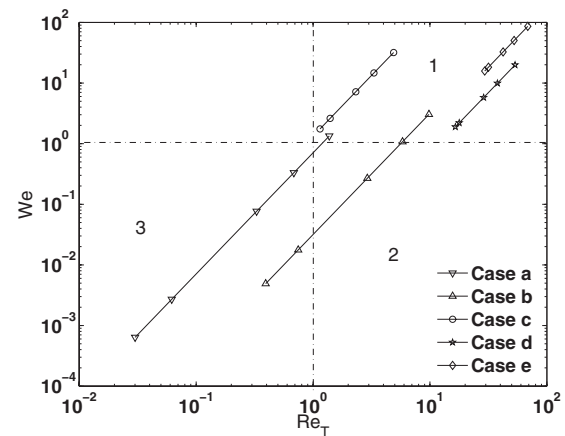
cap bubble. For $R^*=2$, the terminal shape continues to be dimpled ellipsoidal cap, and $\mathrm{Re}_T=4.9$ and We$=32$ (see, Figs. 11–13). While viscous forces are lower than inertia, surface tension forces are even lower. A liquid jet of reduced strength [compared to that in case (b)] is still strong enough to produce an indentation in the rear of the bubble. At $R^*=1$, the bubble is nearly spherical with much reduced indentation at the rear. Here, $\mathrm{Re}_T=3.3$ and We$=14.7$. A reduced role of inertia and an increased role of viscous and surface tension forces result in the decrease in the extent of indentation. With increasing wall proximity, for example, at $R^*=0.55$, the bubble assumes an elongated cylindrical shape with no indentation at the rear. The curvature is slightly smaller on the lower surface than at the top (Fig. 12). The $\mathrm{Re}_T=1.15$ and We$=1.75$. Viscous, inertial, and surface tension forces are of the same order. Progressive change in the curvature at the rear of the drop from negative (concave at $R^*=2$) to positive (convex at $R^*=0.55$) is ascribable to the progressive dominance of surface tension forces as evident from the decrease in We. The decrease in Re_T from $R^*=1$ to $R^*=0.55$ occurs at a lower rate compared to cases (a) and (b). This can be attributed to the larger change in shape and form drag. The deformation factor has a significant change from $R^*=2$ to $R^*=1$, followed by a dramatic increase for $R^*<1$ (Fig. 11). The latter change is akin to a geometric deformation (see dashed-dotted lines in Fig. 11). The elongation of the bubble in the axial direction is due to increased normal stresses.

For case (d), Eo, Mo$=54.4$, 0.0026, $\mathrm{Re}_{T\infty}=60.0$, and the terminal shape in an infinite medium is a spherical cap bubble. For $R^*=2$, the terminal shape continues to be a spherical cap, however, with a small indentation in the rear. Here, $\mathrm{Re}_T=53.5$, We$=20$ (see, Figs. 11–13). The posterior portion of the bubble is relatively flat. At the rim, in the areas of slightly increased curvature, higher surface tension forces accompanied with increased viscous stresses resist further deformation. Thus, a critical balance between inertial, surface tension, and viscous forces is reached resulting in a terminal spherical cap shape with a slight dimple. At $R^*=1$, $\mathrm{Re}_T=37.8$ and We$=10$. Surface tension forces are higher. The lower surface of the bubble is flatter with a much re-

duced indentation and with a slight elongation in the axial direction. The almost spherical cap makes a slow transition to a bullet shaped bubble at $R^* = 0.55$ ($\text{Re}_T = 16.5$ and We $= 1.9$), with a near zero curvature at the bottom (Fig. 12). This is a result of high inertia and surface tension forces. The decrease in Re_T from $R^* = 1$ to $R^* = 0.55$ occurs at a lower rate compared to cases (a), (b), and (c). This is again due to larger deformation. As in case (c), the deformation factor has a significant change from $R^* = 2$ to $R^* = 1$, followed by a dramatic increase for $R^* < 1$ (Fig. 11). This is also akin to a geometric deformation.

For case (e), Eo, Mo$= 277.5$, 0.092, $\text{Re}_{T\infty} = 80.0$, and the terminal shape in an infinite medium is an intermediate spherical-cap–skirted bubble. Viscous forces acting at the rim of the slightly dimpled bubble are strong enough to overcome interfacial tension forces. This results in a skirt. For $R^* = 2$, $\text{Re}_T = 68.7$, We$= 86.1$, and the terminal shape continues to be an intermediate spherical-cap–skirt, although the skirting is very slight (see, Figs. 11–13). At $R^* = 1$, $\text{Re}_T = 52.5$ and We$= 50$. A liquid jet of reduced strength (compared to that at $R^* = 2$) together with the normal stresses introduced by the proximity of walls produce an indentation in the rear of the bubble. This results in a dimpled ellipsoidal shape. At $R^* = 0.55$, $\text{Re}_T = 29.4$, We$= 15.75$, and the shape is a bullet shaped cylindrical bubble with a dimpled rear. Surface tension and viscous forces remain lower than inertial forces. With close proximity of the wall, the normal stresses result in higher deformation (Fig. 12). The decrease in Re_T from $R^* = 1$ to $R^* = 0.55$ occurs at a lower rate compared to all the previous cases. This is again due to larger shape change and corresponding form drag change. The deformation factor as seen from Fig. 11 is akin to a geometric deformation.

The above comprehensive discussions show that wall effects on bubble motion in finite cylinders are complicated and the property values exert important influence.

2. Terminal velocity correlations

In Fig. 14, the variations of dimensionless terminal velocities (U_T/U_{T_∞}) for bubbles in various regimes (see, Table III) are shown as functions of R^*. For $R^* = 2$, the terminal velocities are $\sim 90\%$ of the infinite medium velocities for all cases. This demonstrates the beginning of wall influence. For cases (a) and (b) and $R^* = 0.55$, the slightly elongated bubble and the bubble with a flatter trailing end nearly occlude the flow. For these cases, the ratio $U_T/U_{T_\infty} \approx 0.02, 0.035$, respectively. The deformation factors for these cases, as discussed earlier, are small. Correspondingly, at $R^* = 0.55$, the deformation factors are higher for cases (c), (d), and (e), although, for case (d), the blockage is only slightly lower than for case (b). The ratio U_T/U_{T_∞} are $\approx 0.2, 0.28$, and 0.37, respectively. For the high Eo and high Re systems, corresponding to cases (c), (d), and (e) (see, Table III), the numerically predicted terminal velocities agree well up to $R^* = 1.5$ with the correlation relation given in [1] (Chap. 9, Eq. 9-36). In their notation, $U_T/U_{T_\infty} = 1.13e^{-\lambda}$, $\lambda = \frac{1}{2R^*}$. For $R^* < 1.5$, the deviation from the correlation predictions for these cases increases with decreasing Re_T [see, cases (c), (d), and (e) in Fig. 14].

3. Flow fields

In the earlier sections, wall proximity was noted to slow down the bubble speed and significantly affect bubble defor-
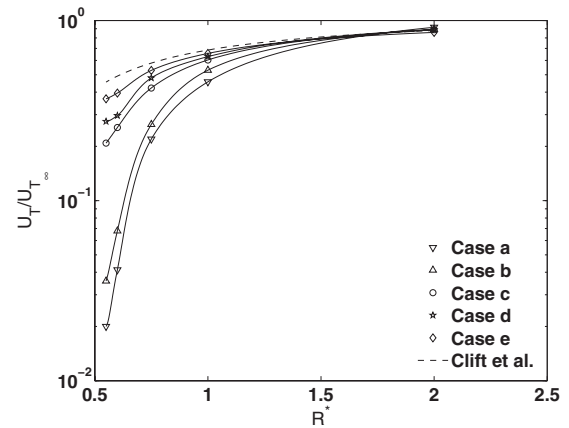

FIG. 14. Wall effects on the terminal velocity of the bubble in different regimes. See Table III for legend details.

mation. In this section, we investigate the detailed nature of the flow fields associated with the bubble motion for cases (b) and (d) (Table III) to further understand the influence of the proximity of the radial wall.

Figure 15 shows the velocity vectors and streamlines for the case (b), for various R^* values when the bubble has attained its terminal state at z_1^*. The flow features are shown both in the laboratory reference frame and in a reference frame moving with the bubble centroid. For case (b), Eo,
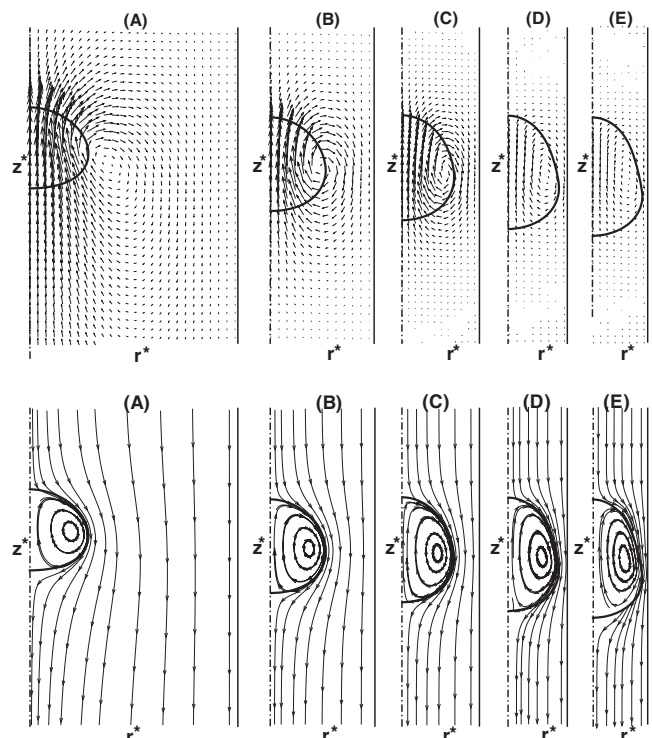

FIG. 15. Velocity vectors and the streamlines for the ellipsoidal bubble at terminal state: Mo$= 0.01$, Eo$= 10.0$. Upper figures are velocity vectors in laboratory reference frame, and the lower ones are streamlines in the frame of reference of the bubble centroid. Here, (A) $R^* = 2$, (B) $R^* = 1$, (C) $R^* = 0.75$, (D) $R^* = 0.6$, (E) $R^* = 0.55$.
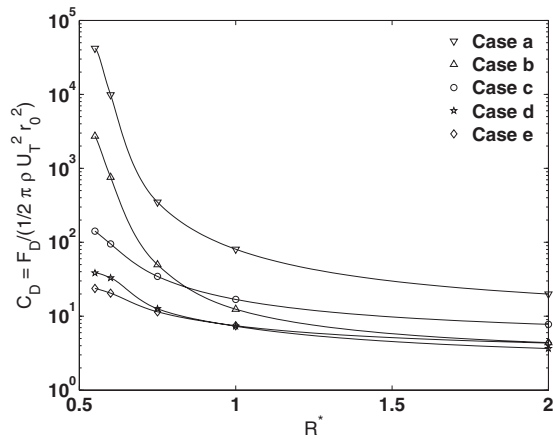
FIG. 16. Values of the drag coefficient C_D for various dimensionless wall distances. See Table III for legend details.

Mo=10, 0.01, $\text{Re}_{T\infty}$=11.0, and the terminal shape in an infinite medium is ellipsoidal. We choose to examine flow fields for five different R^* values of 2, 1, 0.75, 0.6, and 0.55. The figures for the different R^* values are noted by Figs. 15(A)–15(E). The value of H^* is fixed at 8 as before. With increasing wall proximity, the bubble becomes nearly spherical at R^*=1, experiences a slight elongation along the axial direction at R^*=0.75, followed by a further elongation along the axial direction at R^*=0.6, culminating as an elongated
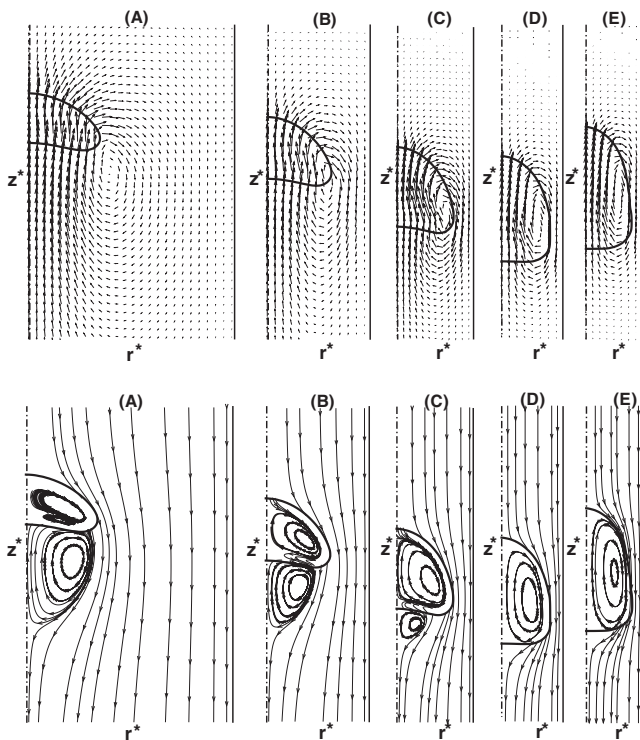

FIG. 17. Velocity vectors and the streamlines for the intermediate spherical-cap–skirted bubble at the terminal state: Mo=2.6 $\times 10^{-3}$, Eo=54.4. Upper figures are velocity vectors in laboratory reference frame, and the lower ones are streamlines in the frame of reference of the bubble centroid. Here, (A) R^*=2, (B) R^*=1, (C) R^*=0.75, (D) R^*=0.6, (E) R^*=0.55.
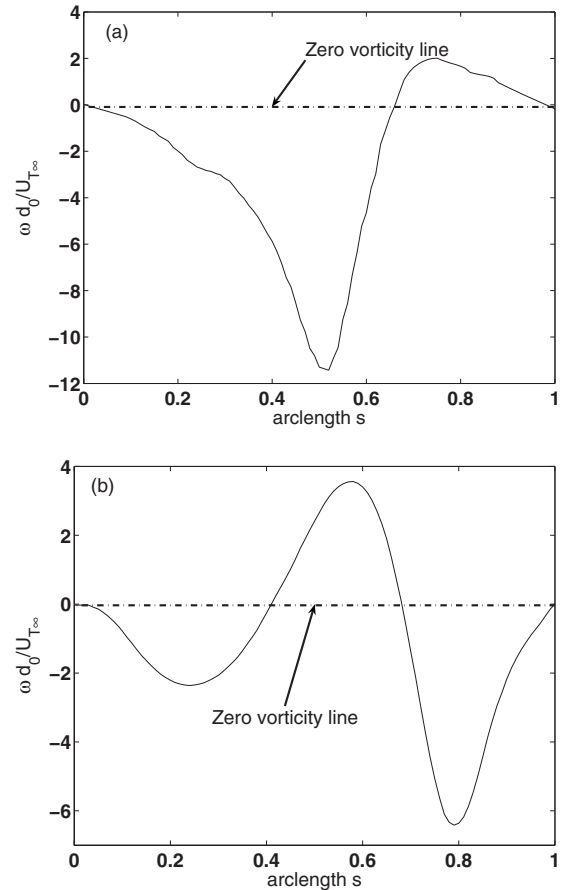

FIG. 18. Nondimensional vorticity at the bubble surface at terminal state for two different R^* values: (a) R^*=2 and (b) R^*=0.55. Here, Mo=2.6×10^{-3}, Eo=54.4 and this corresponds to case (d) in Table III. Dashed–dotted line denotes zero vorticity.

bubble whose trailing end is flatter while the leading end is sharper at R^*=0.55. The corresponding terminal Re_T are 9.8, 5.8, 2.9, 0.75, and 0.4. The reduction in Re_T is directly due to reduction in U_T which is caused by increased drag. The total drag coefficient, C_D, increases with decreasing R^* as would be expected, and as seen in Fig. 16, its value changes from 4.4 at R^*=2 to 2720 at R^*=0.55. The bubble interior experiences a vortical motion due to the slip of the liquid with respect to the bubble surface which then entrains the gas inside the bubble. Since the viscosity ratio of the bubble to the bulk fluid is almost zero (=0.01), the vortex inside the bubble resembles the Hill vortex [49]. With increasing proximity of the wall, the internal vortex strength diminishes, vortical loops are longer to accommodate the shape deformation. There is no flow separation either on the inside or on the outside of the bubble. It is evident from Figs. 15(A)–15(E) that flow is experiencing increasing blockage. Also evident from the velocity vector plots is the reduced jet strength in the rear of the bubble as the radial wall is brought closer.

Figure 17 shows the velocity vectors and streamlines for the case (d), for various R^* values when the bubble has attained its terminal state at z_1^*. The flow features are again shown both in the laboratory reference frame and in a refer-
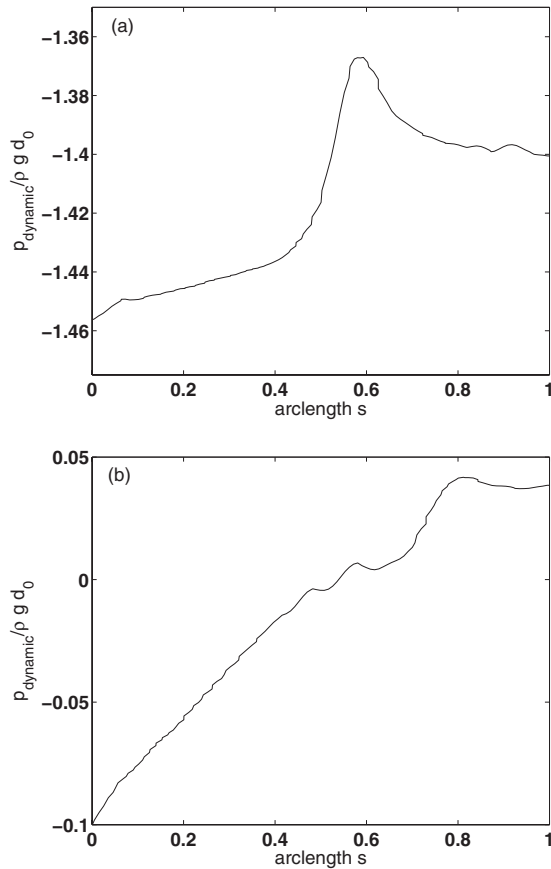
FIG. 19. Dynamic pressure contours on the bubble surface at terminal state for two different R^* values: (a) $R^*=2$ and (b) $R^* =0.55$. Here, $Mo=2.6\times10^{-3}$, $Eo=54.4$ and this corresponds to case (d) in Table III.
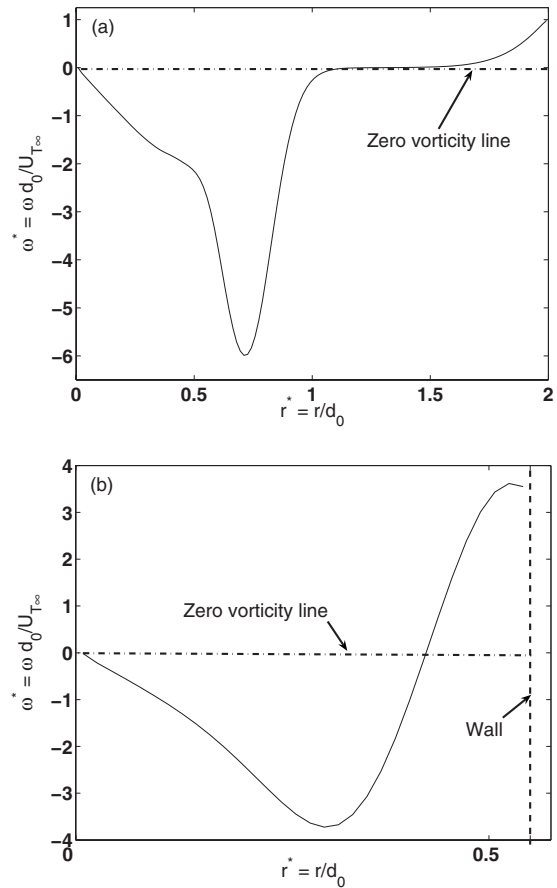

FIG. 20. Cross-sectional plots of the nondimensional vorticity at transverse cross-sectional planes located slightly below the lower surface of the bubble at terminal states for two different R^* values: (a) $R^*=2$ and (b) $R^*=0.55$. Here, $Mo=2.6\times10^{-3}$, $Eo=54.4$, and this corresponds to the case (d) in Table III.

ence frame moving with the bubble centroid. For case (d), Eo, Mo=54.4, 0.0026, $Re_{T\infty}=60.0$, and the terminal shape in an infinite medium is a spherical cap bubble. The figures for the different R^* values are indicated by Figs. 17(A)–17(E). For $R^*=2$, the terminal shape is a spherical cap, however, with a slight indentation in the rear. At $R^*=1$, the lower surface of the bubble is flatter with a much reduced indentation and with a slight elongation in the axial direction. At $R^*=0.75$, the bubble is increasingly squeezed, the posterior of the bubble becoming flatter. At $R^*=0.6$ and 0.55, the bubble deforms into a bullet shape with a flat bottom. The corresponding terminal Re_T's are 53.5, 37.8, 28.8, 17.8, and 16.5. Evidently, the flow fields are in the high Reynolds number regimes. At $R^*=2$, the flow field is vigorous and is accompanied by flow separation and recirculation at the rear. The slip of the liquid with respect to the bubble surface induces vigorous internal vortex motion, and a secondary internal vortex is noted as a result of flow reversal on the surface of the bubble. The strength of the secondary vortex motion is weaker. With increasing closeness of the radial wall, at $R^*=1$ and 0.75, the strength of the recirculating vortices on the outside of the bubble becomes progressively weaker, accompanied by reductions in recirculating wake volumes. The secondary internal vortex motion is also getting weaker, and at $R^*=0.75$ is barely discernible. At R^*

=0.6 and 0.55, with essentially flat lower boundaries, the external recirculation and the secondary internal vortical motions are absent. However, the primary internal vortices are well defined, vortical lines are stretched to accommodate deforming shapes. There is increased blockage of the flow. The total drag coefficient, C_D, as seen in Fig. 16, increases with decreasing R^* as would be expected, and its value changes from 3.7 at $R^*=2$ to 38.4 at $R^*=0.55$.

In Fig. 18, the nondimensional bubble surface vorticity, $\omega^*=\omega d_0/U_{T\infty}$, where $\omega=\nabla\times\mathbf{u}$, is plotted as a function of arclength s along the bubble surface, $s=0$ at the front-stagnation point and $s=1$ at the rear-stagnation point. The results are presented for values of $R^*=2$ and 0.55. For $R^* =2$, as the fluid flow negotiates the bubble surface, the vorticity becomes increasingly negative, and at $s\approx 0.65$, vorticity switches sign [see, Fig. 18(a)]. Beyond this point, there is considerable accumulation of vorticity at the rear and this is accompanied by vigorous recirculation resulting in an attached eddy. The wall vorticity has negligible effect here. With increasing wall proximity, however, the wall vorticity and the surface vorticity interact. At $R^*=0.55$, as seen from Fig. 18(b), the point of separation is closer to the rear stagnation point, and the positive vorticity resulting in clockwise
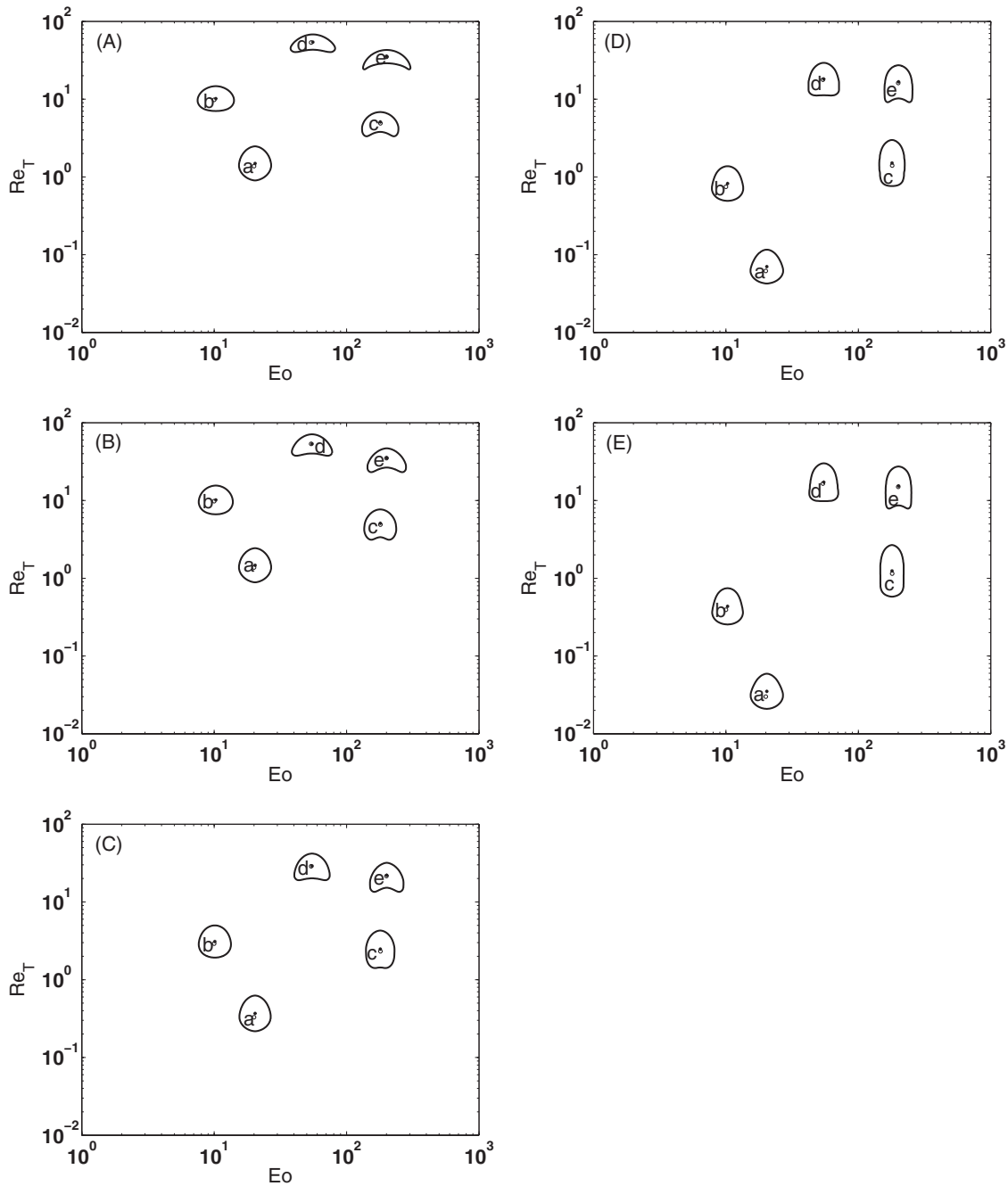
FIG. 21. Bubble shape regimes in the Eo - Re_T space for various wall distances: (A) $R^* = 2$, (B) $R^* = 1$, (C) $R^* = 0.75$, (D) $R^* = 0.6$, (E) $R^* = 0.55$. The Mo values for cases (a)–(e) are given as follows: (a) Mo = 10, (b) Mo = 0.01, (c) Mo = 330, (d) Mo = 0.0026, (e) Mo = 0.092.

recirculation is weaker. At this R^*, the bubble shape is highly deformed from that at $R^* = 2$. Evidently, there is very little accumulation of vorticity and no evidence of recirculation. From $s = 0.4$ to 0.7, the vorticity profile shows a significant influence of the presence of the wall.

In Figs. 19(a) and 19(b), the corresponding dimensionless dynamic pressure variations on the bubble surface are displayed as a function of arclength, for $R^* = 2, 0.55$, respectively. Again, the arclength is measured from the front to the rear stagnation point. The separation point denoting the onset of wake recirculation in Figs. 19(a) corresponds to the point where the surface gradient of pressure changes sign. In Fig.

19(b), there is a uniform increase in pressure from the front to the rear indicating the absence of recirculation region at the rear.

In Figs. 20(a) and 20(b), the nondimensional vorticity at a transverse cross-section plane (normal to the direction of bubble motion) is displayed as a function of $r^* = r/d_0$, for $R^* = 2$, and 0.55. The transverse cross-sectional plane is located slightly below the lower surface of the bubble. The characteristics shown are for the corresponding terminal states. The interaction between wall generated vorticity and the bubble surface induced vorticity are minimal at $R^* = 2$ and are the highest at $R^* = 0.55$ for the cases considered here.

In these figures, the region of negative vorticity denotes the influence of the bubble. On the other hand, vorticity generated at the wall is regarded positive and regions of positive vorticity denote the predominant influence of the cylinder wall. The value of the negative vorticity and the region of influence of the bubble are both higher for the case of $R^* = 2$ [Fig. 20(a)] compared to the case of $R^* = 0.55$ [Fig. 20(b)]. The value of wall vorticity increases for decreasing values of R^*. This is because, as R^* decreases, the downflowing (entrained) fluid has less space to flow which increases the wall shear stress and directly results in an increased level of vorticity at the wall.

4. Bubble shape regimes for various wall proximities

In Figs. 21(A)–21(E), we display the shape regimes for bubbles for $R^* = 2$, 1, 0.75, 0.6, and 0.55, $H^* = 8$ for the wide range of Eo and Mo investigated. These plots which are similar to the shape regime plot given in [1], provide a convenient tool for demonstrating the wide range of bubble behavior under various conditions of wall proximities.

V. CONCLUSIONS

We have described the buoyant axisymmetric rise of a gaseous-bubble in a fluid-filled finite circular cylinder. The motivation has been to examine the proximity of the effects of the cylinder side wall on the bubble behavior. The results have implications for understanding bubble occlusion in cylindrical geometries. The problem has been solved by a hybrid procedure that involves front tracking method together with a level contour reconstruction procedure. This hybrid scheme has been fine-tuned with a "density-weighted" surface tension force distribution procedure. These eliminate interfacial numerical instabilities for flows involving high surface tension forces coupled with large density and viscosity ratios.

The roles of governing parameters expressed in terms of dimensionless quantities H^*, R^*, Re, We, Eo, Mo, ρ_l/ρ_g, and μ_l/μ_g on bubble behavior in a fluid-filled cylinder have been clearly revealed by this numerical study. For the wide ranges of Eo and Mo considered, results show that bubble behavior for $H^* \geq 8$ and $R^* \geq 3$ resembles that in an unbounded (infinite) fluid medium. For a fixed H^* and for $R^* < 3$, wall effects become increasingly significant. Wall proximity increases the total drag on the bubble leading to a slow down of the motion and pronounced change in shape. Under certain conditions bubble deformation is such as to occlude the flow. Under certain other conditions vigorous circulatory motions exist on the bubble interior and on the exterior. At appropriate conditions secondary internal vortices may appear. The paper provides exhaustive information on bubble deformation and includes maps of shape regimes.

In a future study, the effect of the proximity of the top boundary will be explored.

[1] R. Clift, J. R. Grace, and M. E. Weber, *Bubbles, Drops, and Particles* (Academic, New York, 1978).

[2] D. Bhaga and M. E. Weber, J. Fluid Mech. **105**, 61 (1981).

[3] J. R. Grace and T. Wairegi, in *Encyclopedia of Fluid Mechanics* (Gulf, Houston, 1986), Vol. 3, pp. 43–57.

[4] D. S. Dandy and L. G. Leal, J. Fluid Mech. **208**, 161 (1989).

[5] S. S. Sadhal, P. S. Ayyaswamy, and J. N. Chung, *Transport Phenomena with Drops and Bubbles* (Springer-Verlag, New York, 1997).

[6] M. Sussman and P. Smereka, J. Fluid Mech. **341**, 269 (1997).

[7] J. Magnaudet and I. Eames, Annu. Rev. Fluid Mech. **32**, 659 (2000).

[8] D. Rodrigue, AIChE J. **47**, 39 (2001).

[9] A. Esmaeeli and G. Tryggvason, Phys. Fluids **17**, 093303 (2005).

[10] M. Van Sint Annaland, W. Dijkhuizen, N. Deen, and J. Kuipers, AIChE J. **52**, 99 (2006).

[11] D. P. Cavanagh and D. M. Eckmann, J. Fluid Mech. **398**, 225 (1999).

[12] D. M. Eckmann and V. N. Lomivorotov, J. Appl. Physiol. **94**, 860 (2003).

[13] A. Suzuki and D. M. Eckmann, Anesthesiology **99**, 400 (2003).

[14] J. Zhang, D. M. Eckmann, and P. S. Ayyaswamy, J. Comput. Phys. **214**, 366 (2006).

[15] S. Uno and R. C. Kintner, AIChE J. **2**, 420 (1956).

[16] T. Z. Harmathy, AIChE J. **6**, 281 (1960).

[17] M. Coutanceau and P. Thizon, J. Fluid Mech. **107**, 339 (1981).

[18] R. Krishna, M. I. Urseanu, J. M. van Baten, and J. Ellenberger, Int. Commun. Heat Mass Transfer **26**, 781 (1999).

[19] L. Chen, S. V. Garimella, J. A. Reizes, and E. Leonardi, J. Fluid Mech. **387**, 61 (1999).

[20] S. Shin and D. Juric, J. Comput. Phys. **180**, 427 (2002).

[21] S. Shin, S. I. Abdel-Khalik, V. Daru, and D. Juric, J. Comput. Phys. **203**, 493 (2005).

[22] S. O. Unverdi and G. Tryggvason, J. Comput. Phys. **100**, 25 (1992).

[23] J. U. Brackbill, D. B. Kothe, and C. Zemach, J. Comput. Phys. **100**, 335 (1992).

[24] D. J. Torres and J. U. Brackbill, J. Comput. Phys. **165**, 620 (2000).

[25] G. Tryggvason, B. Bunner, A. Esmaeeli, D. Juric, N. Al-Rawahi, W. Tauber, J. Han, S. Nas, and Y. J. Jan, J. Comput. Phys. **169**, 708 (2001).

[26] S. Osher and R. P. Fedkiw, J. Comput. Phys. **169**, 463 (2001).

[27] M. Sussman, A. S. Almgren, J. B. Bell, P. Colella, L. H. Howell, and M. L. Welcome, J. Comput. Phys. **148**, 81 (1999).

[28] D. Jacqmin, J. Comput. Phys. **55**, 96 (1999).

[29] C. W. Hirt and B. D. Nichols, J. Comput. Phys. **39**, 201 (1981).

[30] R. Scardovelli and S. Zaleski, Annu. Rev. Fluid Mech. **31**, 576 (1999).

[31] A. J. James and J. Lowengrub, J. Comput. Phys. **201**, 685 (2004).

[32] M. Sussman and E. G. Puckett, J. Comput. Phys. **162**, 301 (2000).

[33] R. J. Leveque and Z. L. Li, SIAM J. Sci. Comput. (USA) **18**, 709 (1997).

[34] L. Lee and R. J. Leveque, SIAM J. Sci. Comput. (USA) **25**, 832 (2003).

[35] H. S. Udaykumar, L. Tran, D. M. Belk, and K. J. Vanden, J. Comput. Phys. **186**, 136 (2003).

[36] S. P. Quan and D. P. Schmidt, J. Comput. Phys. **221**, 761 (2007).

[37] B. E. Griffith and C. S. Peskin, J. Comput. Phys. **208**, 75 (2005).

[38] P. Swarztrauber and R. Sweet, Report No. NCAR TN/IA-109, 1975 (unpublished).

[39] A. Prosperetti, in *Drop-Surface Interactions* (Springer, New York, 2002).

[40] J. B. Bell, P. Colella, and H. M. Glaz, J. Comput. Phys. **85**, 257 (1989).

[41] J. B. Bell and D. L. Marcus, J. Comput. Phys. **101**, 334 (1992).

[42] A. S. Almgren, J. B. Bell, and W. G. Szymczak, SIAM J. Sci. Comput. (USA) **17**, 358 (1996).

[43] E. G. Puckett, A. S. Almgren, J. B. Bell, D. L. Marcus, and W. G. Rider, J. Comput. Phys. **130**, 269 (1997).

[44] P. Colella, J. Comput. Phys. **87**, 171 (1990).

[45] P. Wesseling, *An Introduction to Multigrid Methods* (Wiley, New York, 1992).

[46] J. G. Hnat and J. D. Buckmaster, Phys. Fluids **19**, 182 (1976).

[47] T. Bonometti and J. Magnaudet, Phys. Fluids **18**, 052102 (2006).

[48] H. D. Mendelson, AIChE J. **13**, 250 (1967).

[49] G. Batchelor, *An Introduction to Fluid Mechanics* (Cambridge University Press, Cambridge, 1967).